Advanced Demisable Technologies for Satellite Structures: Hybrid Demisable Joints and PVD-Based Coatings

Anna Jasmin Theobald[1], Isil Sakraker Özmen[1], Ronja Anton[2], Simon Huembert[1], Lars Wolfgramm[1], Helge Seiler[1], Thorn Schleutker[3], Ali Gülhan[3], Uwe Schulz[1]

(1) DLR Institute of Structures and Design, Pfaffenwaldring 38-40, 70569 Stuttgart, Germany, Email: Jasmin.Theobald@dlr.de, isil.sakraker@dlr.de, simon.huembert@dlr.de, lars.wolfgramm@dlr.de, helge.seiler@dlr.de
(2) DLR, Institute of Materials Research, High Temperature and Functional Coatings Department, Linder Hoehe 51147 Cologne Germany, Email: ronja.anton@dlr.de, uwe.schulz@dlr.de
(3) DLR, Institute of Aerodynamics and Flow Technology, Supersonic and Hypersonic Technologies Department, Linder Hoehe, 51147 Cologne Germany, Email: ali.guelhan@dlr.de, thorn.schleutker@dlr.de

ABSTRACT

The rapid growth of artificial satellites calls for sustainable deorbiting strategies to reduce space debris. This study combines hybrid demisable joints and physical vapor deposition (PVD)-based coatings to enhance satellite disintegration during re-entry. The DLR Institute of Structures and Design developed additively manufactured joints, integrating 3D-printed PEI and CF-PEEK materials with shape memory alloys (SMA) and compression springs, designed for high-altitude breakup and validated through tests and simulations. Meanwhile, the DLR Institute of Material Research employs PVD-based catalytic coatings on high-melting-point metals like V4A stainless steel to improve heat absorption and promote thermal failure. Magnetron sputtered Al, Si, Cr, or NiAl coatings, combined with a copper layer, encourage rapid oxide formation during re-entry. High-temperature lab tests and wind tunnel experiments validate these coatings' performance under extreme conditions. Together, these approaches offer complementary solutions for safer, more effective satellite demise.

1 INTRODUCTION

The exponential increase in the number of manmade objects in Earth orbits has to be smartly managed, if we do not want to imprison ourselves in our planet in the near future. Every month several dozen new satellites are launched, which contributes eventually to the total amount space debris. Design-for-Demise (D4D) is an engineering approach that aims for intentional disintegration of satellite components during atmospheric re-entry, reducing the risk of surviving debris reaching Earth’s surface. Traditional satellite designs prioritize durability and longevity, however D4D shifts the focus toward controlled fragmentation and enhanced disintegration during re-entry. This requires carefully selecting materials and structural configurations that fail predictably under high heat and aerodynamic forces. Key strategies include using lower-melting-point materials, engineered joints that trigger early breakup, and specialized coatings that promote thermal degradation.

This paper focuses on demisable joints for early break-up of satellite primary structures (Section 2) and special coatings for increased demisability (Section 3). By enabling higher-altitude fragmentation, D4D increases the exposure of the inner critical elements such as tanks or reaction wheels to high-temperature plasma flows, accelerating their demise, whereas special coatings can be applied on any kind of structural component for overall improved degradation. All the presented efforts in this paper are part of German Aerospace Center’s (DLR) TEMIS-DEBRIS project.

2 DEMISABLE JOINT

The design for demise triggers early disintegration of primary satellite structures, initiating breakup at higher altitudes than natural disintegration would allow. This extends exposure to high-temperature plasma flows, increasing the likelihood of complete demise of the satellite.

Since 2020, the DLR Institute of Structures and Design has been developing high-altitude breakup concepts [1,11]. As part of DLR’s TEMIS-DEBRIS project, this research expands on previous studies by investigating the joining of thin plates, which are widely used in primary and secondary satellite structures, broadening the scope of re-entry behaviour analysis beyond sandwich structures.

2.1 DEMISABLE JOINT DESIGN

Eu:CROPIS (Euglena and Combined Regenerative Organic-Food Production in Space) is a DLR satellite launched in December 2018. It operates in a Sun-synchronous orbit at 575 km altitude, with a compact design of 1.1 m in height, 1 m in diameter, and a mass of 250 kg. Its primary structure consists of 1 mm thick plates and 2 mm thick brackets joint by M5 screws, which serve as the basis for the development of the demisable joint presented in this work [2].

As the aerodynamic forces at high altitudes (>100 km) are insufficient to separate a loosened joint, the goal is to design a demisable joint that self-triggers a separation mechanism, ensuring the plates fully disconnect [1]. Therefore, the demisable joint is designed with a passive, temperature-triggered ejection mechanism. The activation temperature is set between 200–250 °C, exceeding the maximum temperature the satellite experiences during its orbital life, thereby preventing premature activation.

During atmospheric re-entry the demisable washer of the designed screw connection is positioned on the outside of the satellite and softens earlier than the other components due to its maximizing exposure to high-enthalpy flows. As it degrades, the spring can release its force, pushing the plate outward and pulling the screw through the plate to the inside of the satellite. Additionally, a radius difference between the upper and lower plates ensures that the spring presses only against the upper plate. This mechanism not only releases the screw but also ensures the simultaneous separation of the plates.

In the design the two plates can either be directly connected to each other or joined at an angle via a bracket. However, since the plate and bracket are thin structures with nearly identical thicknesses, the same ejection mechanism applies. Therefore, the plate/bracket connection, as seen in Figure 2.1, is used as a representative case in the following discussion.

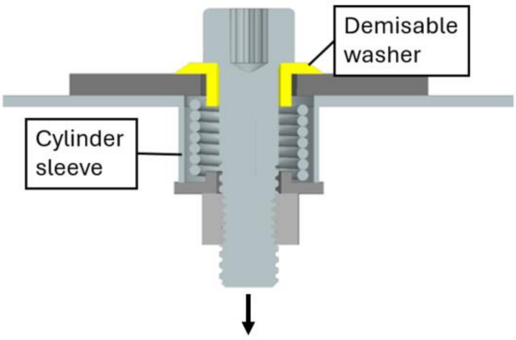

Figure 2.1 Demisable joint concept for thin plates with indicated ejection direction.

2.2 MATERIAL SELECTION

The demisable joint design utilizes materials from the reference satellite, with brackets and plates made of Aluminium 7075 and the screw, nut, and non-demisable washer composed of Titanium Grade 5. Consequently, suitable materials must be selected for the demisable washer and cylindrical sleeve to ensure controlled disintegration during re-entry.

As taken out of previous research done at DLR high-performance thermoplastics PEEK (PolyEtherEtherKetone), which exhibits semi-crystallinity, and PEI (PolyEtherImide), an amorphous thermoplastic, have been identified as promising materials for the demisable washer and the cylinder [11]. They are certified as space-proof, ensuring their suitability for space applications[3,4]. As can be seen in Table 1 Material properties they feature a lower melting/glass temperature and lower density compared to Aluminum 7075 and Titanium Grade 5, making them ideal for triggering the ejection mechanism.

Since the weakest material defines the load capacity of a bolted connection, CF15-PEI and CF30-PEEK—carbon-fibre-reinforced polymers—were selected for their improved stiffness. The embedded carbon fibres significantly increase strength and stiffness along the fibre direction. An additional advantage is their 3D printability, enabling design customization and infill adjustment for future weight and geometry optimization.

CF15-PEI was selected as the demisable washer material due to its amorphous structure, which—compared to semi-crystalline PEEK—leads to a more predictable loss of structural integrity under thermal load. The cylindrical sleeve will be 3D printed from CF30-PEEK for weight saving reasons and for future optimization possibilities.

Table 1 Material properties [4-7]

	Aluminium 7075	**Titanium Grade 5**	**CF15 PEI**	**CF30 PEEK**
Melting Temp T_m[°C]	600	1650	-	343
Glass Temp T_g [°C]	-	-	186	143
Density ρ [kg/dm3]	2.8	4.47	1.39	1.41
Tensile Strenth R_m[MPa]	310	828	Orientation XY 93	Orientation XY 169

2.2.1 Extraction Force

The required spring force was experimentally determined by measuring the minimum load needed to pull the screw head through softened CF15-PEI

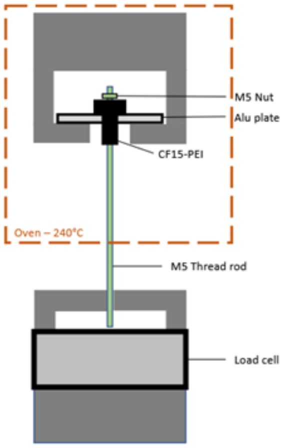

.

Figure 2.2 Test set up for needed spring force determination

Figure 2.3 Demisable washer CF15-PEI before testing difference in height - 4mm on the left, 3mm in the middle and 2mm height on the right.

As shown in Figure 2.3, the tensile tests were conducted using a setup with a temperature-controlled environment. A threaded M5 rod and nut, representing a screw head, was used to pull through softened CF15-PEI.

To replicate activation conditions and define the required spring force for the demisable joint, the screw was pulled through a CF15-PEI washer mounted on an aluminium plate once it reached 220 °C.

The required force was measured across a total ejection path of 10 mm, representing full screw extraction with screw head through both the plate and the bracket. Tests were carried out at two retraction speeds, 10 mm/min and 30 mm/min. To evaluate the influence of washer thickness, 3D printed CF15-PEI washers with thicknesses of 2, 3, and 4 mm were tested, as illustrated in Figure 2.3.

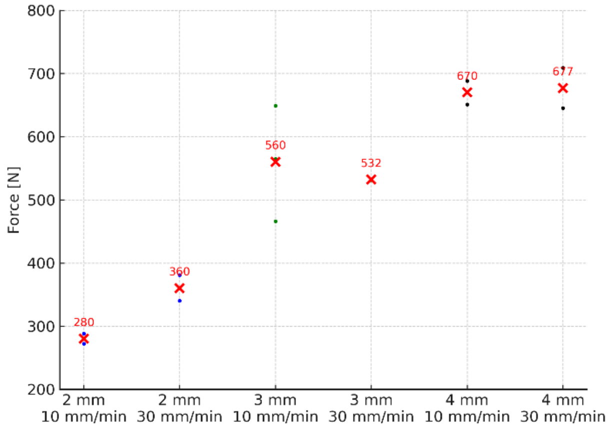

Figure 2.4 Results of the mechanical test to determine minimum needed spring force. The dots indicate the single test results, the cross is the calculated average force.

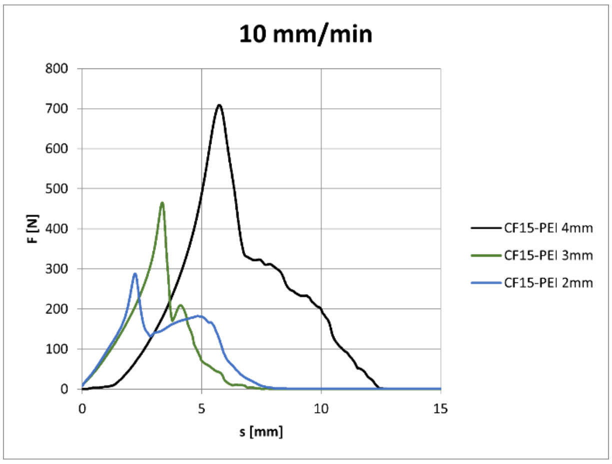

Figure 2.5 Results of the mechanical test to determine minimum needed spring force, one representative result per each testing series. The X-axis indicates the crosshead displacement in mm.

As can be seen with thicker demisable washers the needed force of the spring gets higher. Figure 2.5 shows a smaller second peak, an increase of force during the retraction in the diagram. This is the soften CF15PEI that accumulates during the pulling through process and has to be overtaken. Based on the data presented in Figure 2.4, the hypothesis that retraction velocity affects the required spring force cannot be substantiated.

Due to the limited load-bearing capacity of the thin aluminium plates and brackets, integrating shape memory alloy (SMA) technology is suggested. The shape memory effect in metallic alloys is based on a martensitic phase transformation where the material can be deformed at low temperatures and returns to its original shape upon heating through a reversible transformation. The application of shape memory alloy (SMA) technology offers an effective approach to reducing mechanical stress in the designed demisable joint. The use of an SMA spring was evaluated and should be considered for future work. Currently, no commercially available high quality SMA spring meets the required trigger temperature and spring force needed.

2.2.2 Mechanical Load Capacity

The failure criterion for the joint system was defined by testing the 3D-printed CF15-PEI washer, identified as the system's weakest component. Using the same tensile setup excluding the thermal environment, washers of 2, 3, and 4 mm thickness were evaluated. The force at which the screw head induced material failure was recorded and is presented in Figure 2.6

The experimentally determined force is defined as representing the maximum load in axial direction the demisable CF15PEI washer can withstand before failure - therefor the failure criterion of the designed joint.

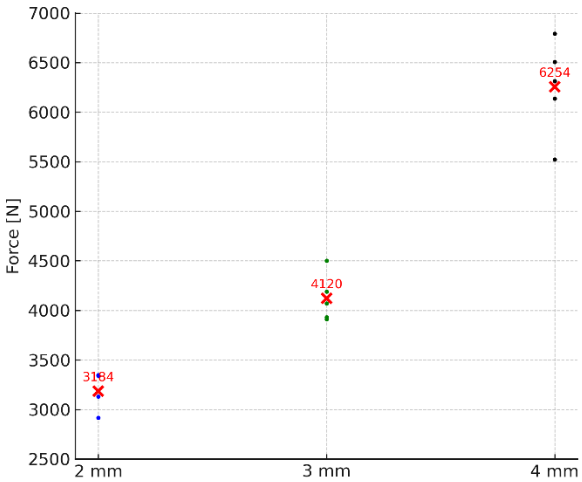

Figure 2.6 Results of the mechanical test to determine maximum axial force depending on demisable washer thicknesses 2, 3, and 4 mm. The dots indicate the single test results, the cross is the calculated average force.

2.3 MAXIMUM FORCE ON DEMISABLE JOINT

2.3.1 Failure criteria

The experimentally determined maximum load capacities of the CF15-PEI demisable washer were implemented in a static structural FEM simulation using ANSYS. This allowed for a detailed stress analysis and the definition of a failure criterion, ensuring consistency between experimental results and numerical modelling. The criterion was established based on the distribution of von Mises stresses.

In order to evaluate the applied loads and define a failure criterion, the resulting stresses were categorized within the simulation environment. A threshold of 93 MPa—matching the tensile strength of CF15-PEI in the corresponding data sheet[6]—was used to distinguish acceptable (green) from critical (yellow to red) stress regions. The legend scale was adapted to best represent the simulated stress field

2 mm height - 3184,5 N

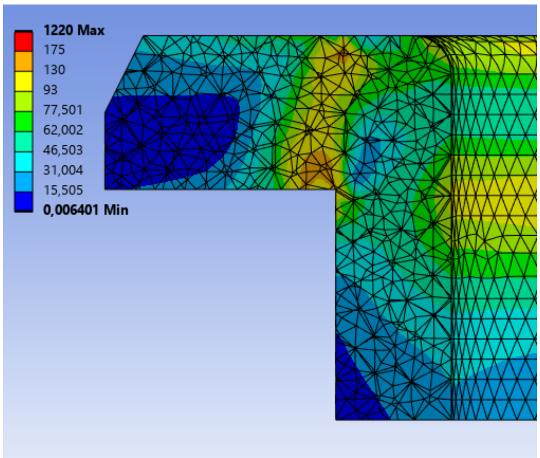

Figure 2.7 *ANSYS failure criterion analysis for a 2 mm thick CF15-PEI washer, showing the cross-sectional distribution of von Mises stresses.*

In the cross section the highest stress concentration occurs at the contact point between the screw head edge and the demisable CF15-PEI washer, with simulation results indicating local stresses exceeding 130 MPa, and peak values around 150 MPa within a limited area. The stress transitions along a defined path from the screw edge to a secondary hotspot at the PEI–aluminium plate interface. Structural integrity in this region requires that stresses remain below 130 MPa, though values up to 150 MPa are tolerable at direct contact zones. No stress values exceeded 175 MPa across the interface.

3 mm height - 4119,7 N

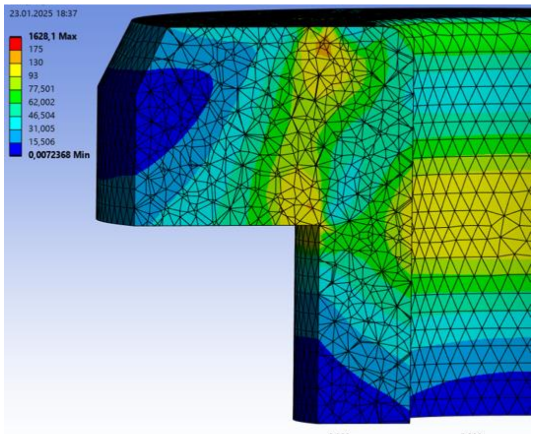

Figure 2.8 ANSYS failure criterion analysis for a 3 mm thick CF15-PEI washer, showing the cross-sectional distribution of von Mises stresses.

Again, two critical stress zones were identified in the CF15-PEI washer—at the contact points with the screw head and bracket plate, this time isolated from each other. In the cross-sectional analysis, the highest stress concentration is observed where the screw edge interfaces with the CF15-PEI washer, with simulated stress values are between 130 and 150 MPa. At the interface between PEI and the aluminium plate, stress levels remain below 130 MPa, aside from isolated peaks reaching 175 MPa.

4 mm height - 6253,7 N

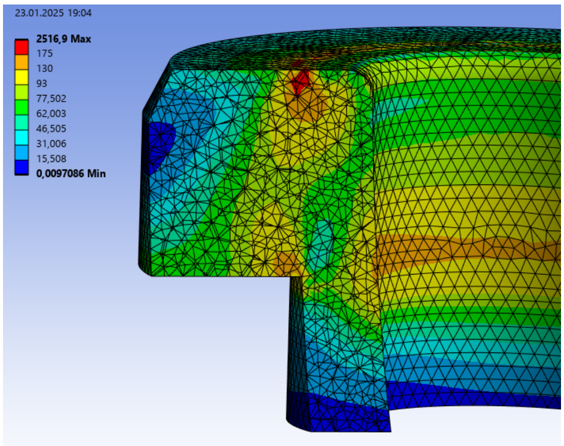

Figure 2.9 ANSYS failure criterion analysis for a 4 mm thick CF15-PEI washer, showing the cross-sectional distribution of von Mises stresses.

As identified in earlier analysis, the critical areas remain at the interfaces between the screw head and CF15-PEI, and between CF15-PEI and the aluminium plate. Maximum stresses of 220 MPa were observed near the screw head, whereas at the CF15-PEI–aluminium interface, stresses remained below the threshold of 150 MPa.

2.3.2 Axial force matrix

To evaluate the structural performance of the joint, a comprehensive analysis was carried out, examining how various modifications to the screw and demisable washer affect the joint's ability to withstand bolt pretension loads. Different design variants were simulated in ANSYS, using 250 N load increments to systematically assess which von Mises stress distribution most closely matched the failure criterion defined in the previous section.

A trade-off must be considered by the user between a higher allowable bolt pretension and the resulting increase in required spring force. As no safety factor has been included in the current analysis, it must be applied individually based on the mission-specific requirements, in accordance with the ECSS regulations [8].

Different screw heads

A larger screw head increases the contact area $A = \frac{\pi}{4} * (d_a^2 - d_i^2)$ between the screw and the CF15-PEI washer, which reduces the surface stress. This leads to a more even distribution of the bolt pretension force, reducing the risk of local material failure and allowing the CF15PEI washer to withstand higher loads. However, a larger screw head requires an increased hole diameter in both plates and a wider CF15-PEI washer. This influences the required spring force for ejection, as a greater volume of softened material must be displaced.

Table 2 Maximum axial force of CF15PEI non demisable washer according to the failure criterium.

Design variations	CF15-PEI height 2 mm [N]	CF15-PEI height 3 mm [N]	CF15-PEI height 4 mm [N]
Mechanical Test M5	3184.5	4119.7	6253.7
Enlarged screw head M5, D=13mm	5000	6000	8500
Different screw diameter:			
M4	2500	3000	4750
M6	4250	4750	7000
M8	5500	7000	9250
Countersunk Screw CF15-PEI height 4mm, M5			5250
Use of multiple screws	Load per screw can be diminished by adding multiple screws		

Different screw diameters

A larger screw diameter automatically means an increase in screw head as well leading to reduce surface pressure, allowing for better force distribution and minimizing local stress. Though an enlarged screw head has a similar effect, such modifications are uncommon and require costly custom parts. Standard larger-diameter screws are not only more accessible and cost-effective, but also mechanically more reliable, being less likely to fail under load. In this design, however, the washer remains the limiting component of the joint.

Multiple screws

By using multiple screws in parallel, the overall load is distributed across several points, thereby reducing the necessary load per individual screw. Since not all conventional joints will be replaced, adding a few additional screws has no significant impact on overall mass. A detailed equation can be found in the VDI 2230 [9].

Countersunk screw

The use of a countersunk screw provides automatic centering, reducing the risk of screw misalignment during ejection—a common failure mode in this configuration. If the screw tilts, it may not pass cleanly through the hole. A countersunk screw applies force at an angle, generating both axial and radial components. While the axial force contributes to clamping, the radial component introduces a spreading effect that displaces the surrounding material sideways. This results in additional stresses and lower tolerated loads, which can be especially problematic in low-strength materials [8].

In the absence of real tensile testing, the maximum load was derived from simulation results of the failure criteria of a 4 mm thick CF15-PEI washer and should be considered a preliminary estimate. This value must be verified through physical testing, especially since the 3D printing process introduces uncertainties in material properties related to layer orientation and inconsistent bonding, which can significantly influence the mechanical response.

2.4 MANUFACTURE AND TESTING

To prove the concept the demisable joint was manufactured and tested in an oven to determine the ejection temperature.

Based on the data sheet specifications [6,10], the demisable washer and cylinder sleeve are 3D printed and assembled with the remaining components as shown in Figure 2.10. During testing, the oven was heated to 240 °C to simulate re-entry conditions, with a thermocouple placed at the outer edge of the demisable washer. All tested concepts activated reliably at ~220 °C (±3 °C), causing a complete disassembly. The functionality of the mechanism was thereby successfully demonstrated. The assembled test setup can be seen in Figures 2.11 and 2.12.

Figure 2.10 Components to build the demisable joint design. The demisable washer is already stacked on the outer aluminum plate.

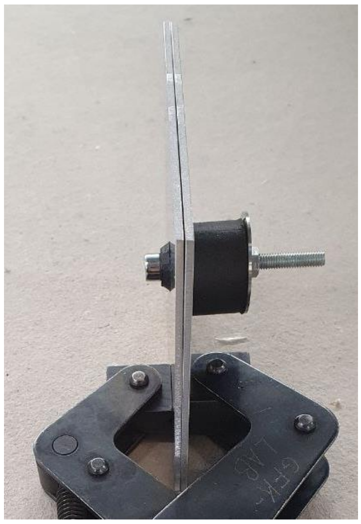

Figure 2.11 Fully assembled demisable joint prior to oven exposure at room temperature (20°C)

2.5 RE-ENTRY SIMULATIONS

To validate the concept, the impact of demisable joints on the demisable behaviour of the satellite during re-entry is investigated using ESA DRAMA software, an object-oriented re-entry simulation tool.

For Eu:CROPIS, the reference satellite, two areas of bolted connections within the satellite—marked in Figure 2.13—are determined. Due to limitations within DRAMA, the joints are modelled as ring-shaped connections between the base satellite structures.

Four simulation scenarios are defined to evaluate the effect of demisable joints:

(1) both the middle and top joint are demisable,
(2) only the middle joint is demisable,
(3) only the top joint is demisable, and
(4) no demisable joint is applied.

Table 3 Fragmentation altitudes for the simulated scenarios, resulting in the decoupling of the connected structural parts.

Scenario	Middle joint [km]	Top joint [km]
No joints demisable	94.5	96.5
Only middle joint demisable	106.5	96.5
Only top joint demisable	94.5	106.5
All joints demisable	107	106.5

Figure 2.12 Demisable joint test in the oven, right joint with disassembled components after ejection at $T_{DemisableWasher}$= 220°C

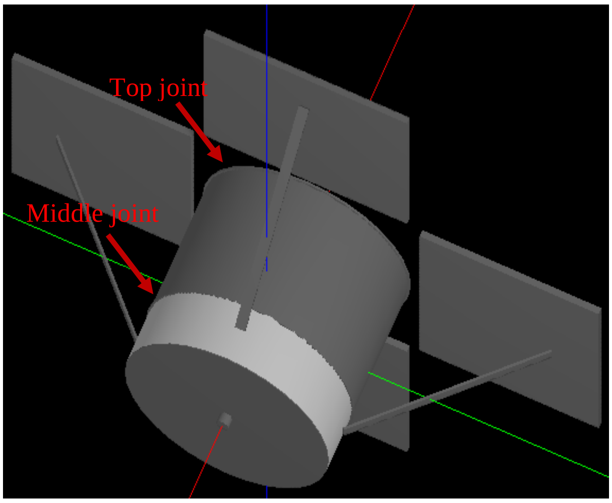

Figure 2.13 Eu:CROPIS with location of the demisable joints

The resulting effects on satellite fragmentation and ground risk are comparing the altitude at which the joints fail depending on the simulated scenario, resulting in the decoupling of the connected structural parts.

To define the joint as demisable within DRAMA, the triggering temperature is set to the targeted and experimentally validated value of 220 °C. When a component reaches its trigger temperature, it separates from the elements it is attached to. This study compares configurations with and without demisable joints. As indicated in Table 3, the breakup altitude increases with the use of the designed demisable joint.

3 PVD-BASED COATINGS FOR ENHANCED DEMISABILITY

Coatings are traditionally employed to functionalize surfaces or provide protection to the underlying components against environmental degradation. Common degradation mechanisms include erosion, corrosion, radiation damage, and various chemical or physical interactions [12]. One prominent example is protective coatings on turbine blades, where the coating's primary role is to shield the substrate from harsh operating environments, ensuring long-term survivability and structural integrity [13,14].

However, in the context of Design-for-Demise (D4D), coatings assume an entirely new and contrasting function. Instead of prolonging lifespan and enhancing durability, coatings are deliberately designed to facilitate rapid degradation and controlled disintegration during re-entry into Earth's atmosphere. Studies indicate that material selection significantly influences the demise behavior of satellite structures and therefore requires focused and intensified investigation [15,16]. For the first time, the functionalization of coatings has been strategically implemented to potentially achieve three objectives: to accelerate the substrate component beneath, to encourage its fragmentation into smaller pieces, and to distribute heat more uniformly. This enables homogeneous and continuous thermal destruction. The approach is included in the DLR project TEMIS-Debris and is described by Gülhan et al. [17].

This study introduces an innovative approach by demonstrating how specifically chosen catalytic and low emissivity coating systems can significantly enhance the demisability of high-melting-point metallic components, exemplified by reaction wheels made from stainless steel AISI 316L. Such a coating strategy supports sustainable material usage, given that the coatings applied are merely a few micrometers thick, thereby minimizing additional mass while maximizing demisability. Magnetron sputtering, a physical vapor deposition (PVD) technique, was selected for this application because of its ability to produce coatings with a dense, columnar-structured morphology and excellent adhesion characteristics. Additionally, magnetron sputtering is compatible with heat-sensitive substrates such as polymers, thus extending the applicability of the proposed coating technology beyond metals to include ceramics, glass, and polymer-based structures. In this study a screening of simple one element coatings Si, Cr and Al is selected. In addition one coating with Ni70Al30 (at.%), further referred to as NiAl. The coatings are known to form protective and slow growing oxide scales at high temperatures Al_2O_3, SiO_2, Cr_2O_3 and Al-Ni-oxides therefore they have potentially a higher survivability during the demise process which prolongs their effect on the substrate material [18-20].

3.1 CHARACTERIZATION STRATEGY

A detailed and systematic characterization approach was implemented to comprehensively evaluate coating systems before and after exposure to oxidation conditions. Initially, scanning electron microscopy (SEM) was utilized to assess the morphology, density, and structural integrity of the as-deposited coatings. Elemental composition and potential impurities were analyzed using energy dispersive X-ray spectroscopy (EDS) coupled with SEM. Subsequently, the coatings underwent controlled high-temperature oxidation tests to study their interaction with the substrate material. Post-oxidation assessments employed SEM and EDS analyses to examine oxide scale formation, interdiffusion processes, and any associated delamination or crack formation phenomena. Additionally, phase composition and crystalline structure of oxide layers were verified through X-ray diffraction (XRD) analyses. This integrated characterization methodology provided critical insights into the suitability and performance of coating systems designed to enhance component demisability under realistic re-entry conditions.

Within the DLR-project TEMIS-Debris, future investigations aim to establish a robust and efficient method for pre-selecting potential coating systems through initial high-temperature oxidation tests conducted under laboratory conditions. These preliminary tests already provide valuable insights into key properties and characteristics, highlighting positive and negative aspects that significantly influence a coating's demisability. Nevertheless, to conclusively assess and validate the actual demise behavior of coatings, subsequent testing under realistic thermal conditions using an arc-heated plasma wind tunnel at approximately 1200 °C remains essential. Samples tested in the plasma wind tunnel will undergo identical characterization procedures (SEM, EDS, XRD) to allow for direct comparison with laboratory-scale results. The overarching goal is to determine the reliability and predictive capability of laboratory-scale tests, ensuring that only the most promising coating systems are selected for resource-intensive, high-fidelity plasma wind tunnel evaluations.

3.2 EXPERIMENTAL

In this study, stainless steel AISI 316L substrates with dimensions of 20 mm × 20 mm × 1 mm were coated using magnetron sputter deposition. The surface of the specimen was grinded up to 1200 grid and cleaned afterwards in an ultrasound bath. The coatings were fabricated utilizing a batch-type magnetron sputtering facility (Z 400, Systec SVS Vacuum Coatings, Karlstadt, Germany) as well as an industrial-scale multisource magnetron sputtering system (IMPAX, Systec SVS Vacuum Coatings, Karlstadt, Germany), Figure 3.1. The coating machines enable homogenous coating thickness all around a component due to a up to three-fold rotation. Moreover, the coater can vary coating composition very widely since 1-4 targets are able to be installed enabling rapid materials development through combinatorial deposition.

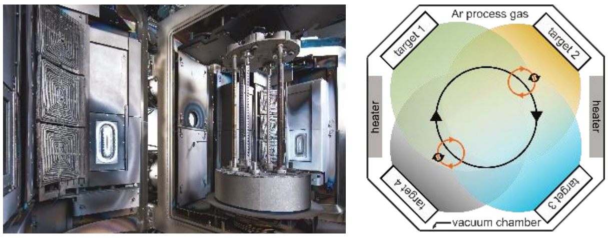

Figure 3.1 left: Industrial-sized industrial-scale multisource magnetron sputtering system ©DLR; right: schematic drawing of the system.

Prior to coating, one side of each specimen underwent surface cleaning and activation via Ar+-ion etching. Dense polycrystalline targets of Si, Al, Cr, Ni70Al30 (at%), Cu, and Ag were used and arranged in a face-to-face configuration. DC sputter deposition was conducted at various target powers to achieve coatings of approximately 20 µm thickness, each with an additional top layer of approximately 100 nm Cu. For a second Al coating, Ag was applied as a 100 nm thick top layer. During the deposition process, the total pressure was maintained at 0.45 Pa in an Ar atmosphere.

Following coating deposition, the coated specimens were subjected to oxidation tests in ambient laboratory air at 1200 °C for a duration of 1 hour. Additionally, one specimen of each coating type was characterized immediately after deposition (as-coated condition). Phase analyses of all specimens were performed using XRD (Bruker D8 Advance, Cu Kα radiation; evaluation software: EVA/Topas 4.2, Bruker AXS, Karlsruhe, Germany). Microstructural analyses were conducted utilizing SEM (DSM Ultra 55, Carl Zeiss NTS, Wetzlar, Germany), equipped with an EDS system (Aztec, Oxford Instruments, Abingdon, UK). The EDS analyses were conducted at an acceleration voltage of 15 kV.

3.3 RESULTS

After deposition, the coating systems exhibited excellent adhesion to the substrate material. Exemplarily, three different coating systems are shown in Figure 3.2. The coatings are dense, with minor impurities such as pores observed particularly in the Al coating. The Ag topcoat appears somewhat inhomogeneous, which can be attributed to the sample preparation process. Thin and relatively ductile layers like Ag are challenging to prepare on a comparably hard stainless steel substrate. The Cr coating clearly demonstrates a distinct columnar structure, which is typical for coatings deposited by PVD methods. The Cu layer on top of the Cr coating is not clearly visible and thus not indicated, as copper is similarly challenging to prepare metallographically due to its high ductility and low hardness. The Si coating is homogeneous and dense. However, in this micrograph, the Cu topcoat experienced delamination, which is again attributed to the metallographic preparation process and does not reflect weak adhesion or compromised performance of the coating system under intended operational conditions.

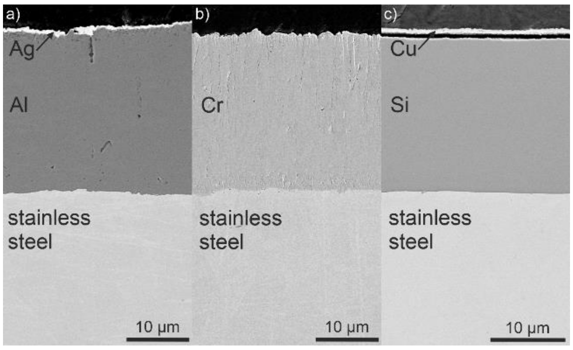

Figure 3.2 SEM-micrographs of as-coated systems; a) Al-coating with Ag topcoat; b) Cr coating with Cu topcoat; c) Si coating with Cu topcoat.

For the oxidation tests, the coated samples were placed into a furnace preheated to approximately 900 °C, and then rapidly heated up to 1200 °C. After exposure for 1 hour at this temperature, the samples were quickly removed from the hot furnace and cooled down rapidly, a process known as quenching.

Figure 3.3 a) depicts the Al coating with an Ag topcoat following oxidation. EDS analysis confirms the formation of an Al_2O_3 oxide layer on the surface. Near the original coating-substrate interface, significant porosity and Al_2O_3 formations are clearly visible, likely resulting from extensive interdiffusion processes between the coating and substrate. The interdiffusion zone (IDZ), marked by an arrow, demonstrates substantial Al diffusion into the substrate, reaching a depth of approximately 200 µm. The original coating combined with the IDZ forms a pronounced Al-enriched zone within the stainless steel substrate. Ag traces are detectable only within the Al_2O_3 oxide layer at the top surface.

Figure 3.3 b) illustrates the Cr coating with a Cu topcoat after oxidation. This coating shows behavior similar to the Al-coating, characterized by the formation of a Cr-enriched IDZ approximately 80 µm thick. The former coating and IDZ collectively form a Cr-rich surface zone within the stainless steel substrate. Cr_2O_3 is detectable on the surface, along with precipitates near the surface region. Cu is not clearly identifiable after oxidation in the SEM only the XRD scans indicate Cu.

Figure 3.3 c) shows the Si coating with a Cu topcoat after 1-hour oxidation at 1200 °C. In contrast to the previously described coating systems, the original interface between coating and substrate is not clearly visible. Si diffusion is observable from the surface down to approximately 150 µm into the stainless steel substrate, without forming a distinct IDZ comparable to the other coating systems. Close to the surface, SiO_2 formations are detectable. The XRD scan clearly reveals cristobalite formation. Additionally, a mixed oxide scale composed of Si, Ni, Cr, Fe, Mn, and Cu is identified at the top surface.

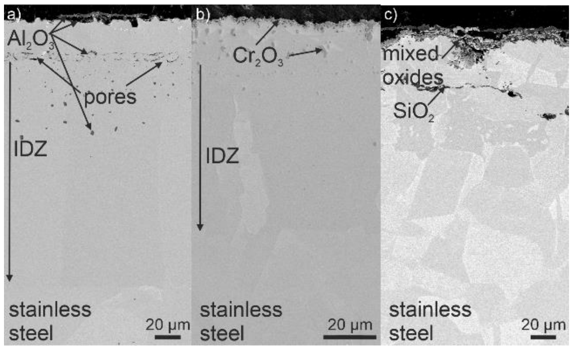

Figure 3.3 SEM-micrographs after 1 hour oxidation at 1200 °C; a) Al coating with Ag topcoat; b) Cr coating with Cu topcoat; c) Si coating with Cu topcoat.

As demonstrated in Figure 3.4, the Al coating with Cu topcoat following oxidation exhibited comparable behaviour to that observed in Figure 3.3 a). The formation of Al_2O_3 is distinctly evident in the EDS mapping. Additionally, the IDZ, measuring approximately 200 µm in thickness, is clearly defined. The mapping further reveals the presence of the three most abundant elements in the steel, namely Fe, Cr and Ni.

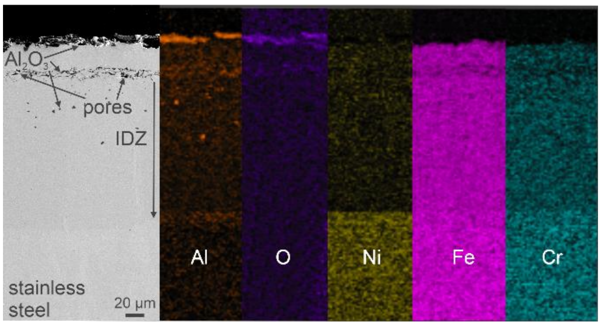

Figure 3.4 SEM-micrograph and EDS-mapping of the Al coating with Cu topcoat after 1 hour oxidation at 1200 °C.

The results of the NiAl coating with a Cu topcoat are displayed in Figure 3.5. The coating performs in a manner analogous to a protective coating. The presence of a continuous thermally grown oxide (TGO) of Al_2O_3 has been identified at the interface between the coating and the substrate, as well as within the cracks of the coating itself. The formation of Al_2O_3 has also occurred at the interface between the coating and the substrate. The EDS mapping reveals that Fe and Cr diffuse up to 10 µm into the coating, while Ni forms an IDZ of about 10-20 µm into the stainless steel. The coating appears to be divided into two compositional parts: Al-rich for the first 10 µm from the surface and Al-poor for the remaining 10 µm. The decrease in Al can be attributed to the formation of Al oxides. In summary, the coating displays an excellent level of adhesion and retains a robust structural integrity.

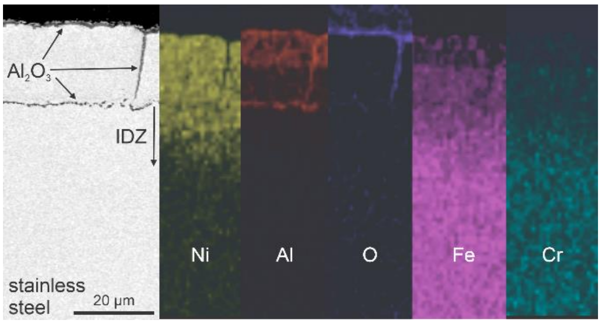

Figure 3.5 SEM-micrograph and EDS-mapping of the NiAl coating with Cu topcoat after 1 hour oxidation at 1200 °C.

3.4 DISCUSSION

Five distinct coating systems were successfully deposited onto stainless steel substrates via magnetron sputtering. All coating systems demonstrated excellent adhesion in their as-coated state and exhibited typical PVD morphology characterized by dense, columnar structures. Similar morphological features for Si-coatings are consistent with findings reported in previous studies [19,21].

Following oxidation tests, the coatings were analysed individually. The Al-based coating systems, regardless of the presence of an Ag or Cu topcoat, behaved similarly (see Figure 3.3 a) and Figure 3.4). The formation of Al_2O_3 on the surface appeared incomplete, lacking full density and continuity. This observation could be attributed to the relatively low melting point of aluminium, potentially causing ruptures in the oxide scale during melting [22]. The formation of a thick IDZ between Al and Fe is explained by the high diffusion coefficients of Fe in Al and Al in Fe, as previously described by Kobayashi et al.[23]. Although intermetallic phases could not be definitively confirmed in the current study, their formation is highly plausible based on literature findings, suggesting that Fe-Al intermetallic may offer a beneficial compromise in melting points—lower than stainless steel but higher than aluminium [22]. Such intermetallic phases may thus enhance heat transfer into the component during the demise process without premature melting.

The Cr-based coating formed a Cr_2O_3 oxide layer accompanied by precipitates near the surface. Given that Cr_2O_3 is known to form volatile species at the test temperatures, partial loss of the oxide layer is likely [24]. The observed chromium diffusion into the stainless steel substrate aligns well with findings reported by Smith [25]. However, chromium diffusion is known to enhance corrosion resistance in stainless steel, indicating limited suitability for demise-promoting coatings [26].

The Si-based coating did not significantly influence substrate oxidation despite rapid Si diffusion into the stainless steel. The formation of a continuous and protective SiO_2 thermally grown oxide (TGO) was not observed. It is evident that the coating and substrate interfaces are no longer distinguishable, which suggests the potential for spallation of the Si coating. This phenomenon can be attributed to the substantial CTE mismatch between the two materials [27,28].

The NiAl coating exhibited considerable potential as an oxidation protective layer by forming a continuous Al_2O_3 oxide scale, consistent with previously reported results [29]. However, significant crack formation within the coating was observed, with cracks being filled by Al_2O_3, aligning with observations made by Muñoz Saldaña et al. [30].

The potential catalytic effects of Cu and Ag topcoats were inconclusive at this stage, primarily due to the extended duration of the oxidation tests.

3.5 SUMMARY AND OUTLOOK

This study aimed at screening various coating systems to improve the demise behaviour of reaction wheels used in satellite applications. Five coating systems, Al+Cu, Al+Ag, Cr+Cu, Si+Cu and Ni70Al30+Cu, were successfully deposited on stainless steel substrates using magnetron sputter deposition. The oxidation behaviour of these coatings was analysed following exposure for 1 hour at 1200 °C, providing insights into coating-substrate interactions and diffusion processes. Strong interdiffusion between coatings and substrate was observed for all coating systems except Ni70Al30+Cu. The NiAl coating provided excellent oxidation protection

Future research within the DLR project TEMIS-Debris will include demise testing of the most promising coating systems under destructive entry-flight simulations in the arc heated wind tunnels of DLR in Cologne. Additionally, laboratory-based pre-screening methods for evaluating coating performance will be developed, facilitating more efficient selection and optimization of coating compositions for subsequent testing campaigns.

4 CONCLUSION

This study presents strategies to improve satellite demisability, combining advanced structural joint design with innovative material coatings. Hybrid demisable joints, integrating 3D-printed thermoplastics and compression spring mechanisms, enable controlled high-altitude breakup, ensuring key components are exposed to intense heat for extended periods. Extensive testing and simulations confirmed the joints' ability to balance structural integrity during launch with predictable failure during re-entry at higher altitudes. Complementing this, PVD-based catalytic coatings accelerate thermal degradation of high-melting-point materials, promoting rapid heat absorption and controlled oxidation. Laboratory and wind tunnel tests validated the coatings' performance, demonstrating reliable thermal failure under extreme conditions. The combined use of demisable joints in primary structures and tailored coatings for all satellite structures offers an effective approach for diverse satellite configurations. This synergy addresses the challenges of reducing surviving debris while maintaining launch and operational reliability. Future work will explore more advanced materials, further optimize joint designs, and extend coating trials to larger structures and more complex components. The results contribute to a growing framework of Design-for-Demise (D4D) strategies essential for ensuring sustainable space operations. By promoting safer satellite disintegration, this research supports international efforts to mitigate space debris and protect orbital environments for future missions.

5 REFERENCES

1. J. J. Patzwald, "Design-for-Demise Concepts with Additively Manufactured Satellite Parts," Master Thesis, DLR & RWTH Aachen University, 2021.

2. Gunter's Space Page, Eu:CROPIS. [Online]. Available: https://space.skyrocket.de/doc_sdat/eu-cropis.htm (accessed: Mar. 25 2025).

3. "Design and evaluation of additively manufactured polyetherimide orbital debris shielding for spacecraft - 1-s2.0-S0734743X24002756-main,"

4. E. Plastics, Technical Data Sheet: TECAFIL PEEK EV CF30 Black - 1.75 mm. [Online]. Available: https://www.ensingerplastics.com/de-de/filamente/tecafil-peek-ev-cf30-black-1-75-mm

5. ThyssenKrupp, Technical Data Sheet: Aluminium Alloy EN-AW-7075. [Online accessed: Mar. 25 2025]. Available: https://datenblaetter.thyssenkrupp.ch/en_aw_7075_0717.pdf

6. 3DXTech, Technical Data Sheet: CarbonX Carbon Fiber Ultem 9085 3D Printing Filament. [Online accessed: Mar. 25 2025]. Available: https://www.3dxtech.com/products/pei-cf15?srsltid=AfmBOoradNlknQB9jgrhhXmNqeVOrQiE5nqze7reqpc0zh63fX7_JUhj

7. "datenblatt-titan-grade-5-eli," [Online accessed: Mar. 25 2025]. Available: https://hwn-titan.com/wp-content/uploads/datenblatt-titan-grade-5-eli.pdf

8. E. Secretariat, Space Engineering: Threaded Fasteners Handbook. Noordwijk, The Netherlands: ESA-ESTEC, Requirements & Standards Section, 2023.

9. VDI 2230 Blatt 1 - Systematische Berechnung hochbeanspruchter Schraubenverbindungen - Zylindrische Einschraubenverbindungen. [Online]. Available: https://www.vdi.de/richtlinien/details/vdi-2230-blatt-1-systematische-berechnung-hochbeanspruchter-schraubenverbindungen-zylindrische-einschraubenverbindungen (accessed: Mar. 25 2025).

10. Department of Biomedical Engineering, University of Basel, PEEK Material Details. Accessed: Mar. 24 2025. [Online]. Available: https://dbe.unibas.ch/en/research/core-facility-3d-print-lab/home/materials/peek-mater/

11. Ring, A.:" Hybrid Demisable Joint Concept for High-Altitude Break-Up of Primary Satellite Structures" Master thesis, DLR & University of Stuttgart, 2023.

12. Tillmann W, Vogli E. (2006). Selecting Surface-treatment Technologies in *Modern Surface Technology*, pp. 1-10

13. Schulz U, Leyens, C., Fritscher, K., Peters, M., Saruhan-Brings, B., Lavigne, O., Dorvaux, J.-M., Poulain, M., Mévrel, Remy, C., M. (2003). Some recent trends in research and technology of advanced thermal barrier coatings. *Aerospace Science and Technology* **7**(1), 73-80

14. Lee KN. (2006). Protective coatings for gas turbines. *The gas turbine handbook* **4**(2)

15. Park S, Neeb D, Plyushchev G, Leyland P, Gülhan A. (2021). A study on heat flux predictions for re-entry flight analysis. *Acta Astronautica* **187**, 271-280

16. Mirko T, Lewis H, Colombo C. (2018). Demisability and survivability sensitivity to design-for-demise techniques. *Acta Astronautica* **145**, 357-384

17. Gülhan; A, Schleutker; T, Goldyn; P, Jack; S, Lemaitre; L, Wartemann V. (2025). Objectives and Achievements of the Space Debris Mitigation Project TEMIS-Debris. Presented at *9th European Conference on Space Debris*, Bonn

18. Bürgel R, Maier, H.J., Niendorf T. (2011). *Handbuch Hochtemperatur-Werkstofftechnik: Grundlagen, Werkstoffbeanspruchungen,*

Hochtemperaturlegierungen und -beschichtungen. Wiesbaden: Vieweg Teubner. 599 pp.

19. Anton R, Leisner V, Watermeyer P, Engstler M, Schulz U. (2020). Hafnia-doped silicon bond coats manufactured by PVD for SiC/SiC CMCs. *Acta Materialia* **183**, 471-483

20. Anton R, Laska N, Schulz U, Obert S, Heilmaier M. (2020). Magnetron Sputtered Silicon Coatings as Oxidation Protection for Mo-Based Alloys. *Advanced Engineering Materials* **22**(7), 2000218

21. Anton R, Leisner V, Schulz U, Obert S, Heilmaier M. (2019). Oxidation protection for Mo-based alloys by magnetron sputtered Si-based coatings. Presented at *Beyond Nickel-Based Superalloys III*, Nara, Japan

22. Massalski T. (1990). Binary Alloy Phase Diagrams, Second edi, Materials Information Soc. *Materials Park, OH*

23. Kobayashi S, Yakou T. (2002). Control of intermetallic compound layers at interface between steel and aluminum by diffusion-treatment. *Materials Science and Engineering: A* **338**(1), 44-53

24. Graham HC, Davis HH. (1971). Oxidation/Vaporization Kinetics of Cr2O3. *Journal of the American Ceramic Society* **54**(2), 89-93

25. Smith AF. (1975). The Diffusion of Chromium in Type 316 Stainless Steel. *Metal Science* **9A**(1), 375-378

26. Ostwald C, Grabke HJ. (2004). Initial oxidation and chromium diffusion. I. Effects of surface working on 9–20% Cr steels. *Corrosion Science* **46**(5), 1113-1127

27. Mertens A, Reginster S, Paydas H, Contrepois Q, Dormal T, et al. (2014). Mechanical properties of alloy Ti–6Al–4V and of stainless steel 316L processed by selective laser melting: Influence of out-of-equilibrium microstructures. *Powder Metallurgy* **57**(3), 184-189

28. Okada Y, Tokumaru Y. (1984). Precise determination of lattice parameter and thermal expansion coefficient of silicon between 300 and 1500 K. *Journal of Applied Physics* **56**(2), 314-320

29. Choi SC, Cho HJ, Kim YJ, Lee DB. (1996). High-temperature oxidation behavior of pure Ni3Al. *Oxidation of Metals* **46**(1), 51-72

30. Muñoz Saldaña J, Schulz U, Mondragón Rodríguez GC, Caceres-Diaz LA, Lau H. (2018). Microstructure and lifetime of Hf or Zr doped sputtered NiAlCr bond coat/7YSZ EB-PVD TBC systems. *Surface and Coatings Technology* **335**, 41-51